Chapter 5
Basic Principles of Neutron Radiography and Tomography

Tushar Roy

5.1 Introduction

Neutron imaging was first used successfully in 1935, shortly after the discovery of neutron by James Chadwick. Since then it has developed manifold and is now used in research for a wide range of applications. With the emergence of digital detectors with better spatial and temporal resolution, neutron imaging has developed into a valuable and reliable technique for materials research.

Neutron imaging is a general term used for the process of forming an image on a detector medium using neutrons as radiation source. More commonly, conventional neutron radiography uses attenuation in the medium or absorption contrast to form the image. Neutron imaging, in general, can also be used with other interaction modalities like refraction, scattering, diffraction, etc.

5.2 Imaging with Radiation

When radiation passes through an object, it interacts with matter and suffers loss in its intensity. The beam is said to undergo attenuation in the medium. The loss in intensity is given by the well-known Beer-Lambert law:

$$I(x) = I_0 \mathrm{e}^{-\mu x} \tag{5.1}$$

where I_0 is the incident intensity, $I(x)$ is the transmitted intensity, μ is the linear attenuation coefficient of the medium and x is the thickness of the medium. Here it is implicitly assumed that μ is constant. For non-uniform μ, Eq. 5.1 may be expressed

T. Roy (✉)
Technical Physics Division, Bhabha Atomic Research Centre, Mumbai, India
e-mail: tushar@barc.gov.in

D. K. Aswal et al. (eds.), *Neutron Imaging*,
https://doi.org/10.1007/978-981-16-6273-7_5

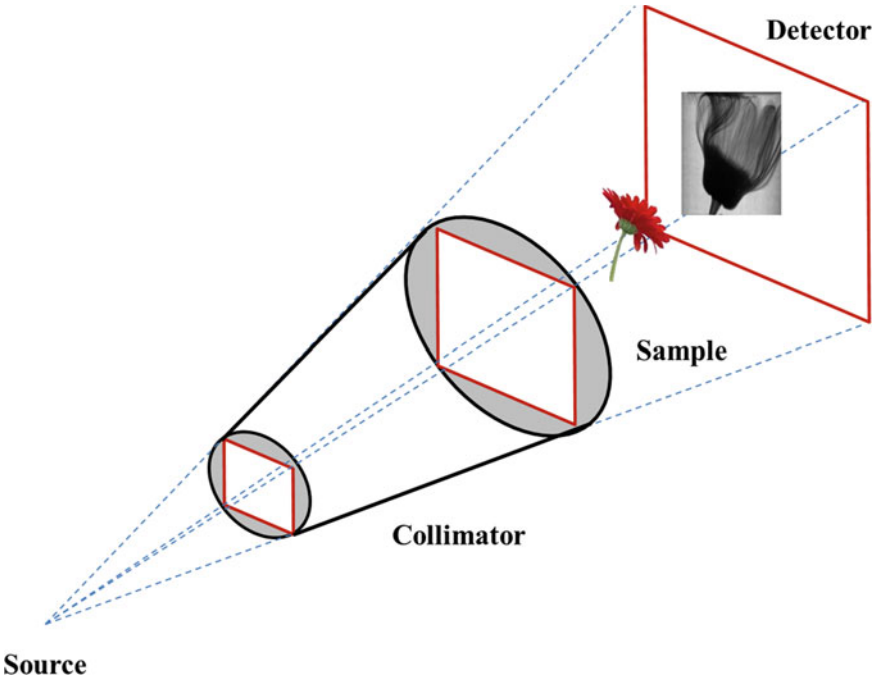

Fig. 5.1 Schematic configuration for radiography

as

$$I = I_0 \mathrm{e}^{-\int \mu(x)\mathrm{d}x} \tag{5.2}$$

where the integral is over the path traversed by the radiation.

The Beer-Lambert law forms the basis of imaging with radiation. When the incident radiation after transmission through an object is captured on a detector/screen, it forms a two-dimensional image of the three-dimensional object. This is known as the *radiograph* of the object (Fig. 5.1).

5.3 Neutron Radiography

The interaction of neutrons [1] with nuclei of target material under investigation is governed by the cross section (σ), which is defined as the probability of neutron-nuclei interaction. The cross section for a given nuclear interaction is also dependent on other factors, such as the energy of the neutron, the type of interaction, and the stability of the target nucleus. The intensity of a neutron beam passing through a

target material of thickness x is expressed as

$$I(x) = I_0 e^{-\Sigma_t x} = I_0 e^{-N\sigma_t x} \tag{5.3}$$

where I_0 is the incident intensity, I is the transmitted intensity and x is the thickness of the medium. The total macroscopic cross section (Σ_t) is defined as

$$\Sigma_t = N\sigma_t = \sigma_t \rho N_A / A \tag{5.4}$$

where N is the atom density of the target material, σ_t is the total microscopic cross section, ρ is the material density, N_A is the Avagadro's number and A is the atomic weight. Depending on the different reaction channels, the total cross-section (σ_t) defines the overall probability of neutron reaction with the target nucleus, and is expressed as

$$\sigma_t = \sigma_{\text{el}} + \sigma_{\text{inel}} + \sigma_c + \sigma_f + \cdots \tag{5.5}$$

where σ_{el} is elastic scattering cross section, σ_{inel} is inelastic scattering cross section, σ_{c} is capture cross section (may be split into individual capture reactions) and σ_{f} is fission cross section.

Comparing Eqs. 5.1 and 5.3, it may be noticed that the attenuation of neutrons in the medium is given by total macroscopic cross-section Σ_t which is a more convenient nomenclature used in case of neutrons, whereas the linear attenuation coefficient μ is conventionally used for X-ray or gamma interaction. For composite materials, Eq. 5.3 may be written as

$$I(x) = I_0 e^{-\int \Sigma_t(x)\mathrm{d}x} = I_0 e^{-\int N\sigma_t(x)\mathrm{d}x} \tag{5.6}$$

Equation 5.6 is the governing principle of neutron radiography. The transmitted neutron intensity is incident on a neutron converter screen (or neutron scintillator) which generates light photons that can be recorded on a film or digital detector like CCD.

Thermal Neutron Radiography requires a collimated beam of thermal neutrons with intensity typically in the range of 10^6–10^8 n/cm^2 s. The neutron beam interacts with the sample and is attenuated in the sample depending on their interaction. Light elements such as hydrogen (H), lithium (Li), and boron (B) and some heavy elements such as gadolinium (Gd), cadmium (Cd), and dysprosium (Dy) have a very high attenuation coefficient for thermal neutrons. On the other hand, materials like lead (Pb), iron (Fe), aluminum (Al), zirconium (Zr) have very low attenuation coefficient for thermal neutrons. Neutron radiography is therefore useful in imaging objects containing hydrogen or light elements such as plastic, rubber, polymer even when shielded by heavy elements like lead.

5.4 Line Integrals and Projection Image

In the expression for intensity (Eq. 5.2), the integral on the right is a line integral which represents the integral of the linear attenuation coefficient of the object along a line. In the context of neutron radiography, the line integral represents the total attenuation suffered by the incident neutron beam as it travels in a straight line through the object.

In Fig. 5.2, the object is represented by the function $f(x, y)$. In the co-ordinate system shown in figure,

$$\begin{aligned} s &= x\cos\theta + y\sin\theta \\ t &= -x\sin\theta + y\cos\theta \end{aligned} \tag{5.7}$$

We define the line integral as

$$P_\theta(s) = \int\limits_{(s,\theta)\text{line}} f(x, y)\mathrm{d}t \tag{5.8}$$

where the line (s, θ) is the line along which the integral is evaluated (or the path of the neutron beam through the object) and is given by the equation

$$s = x\cos\theta + y\sin\theta \tag{5.9}$$

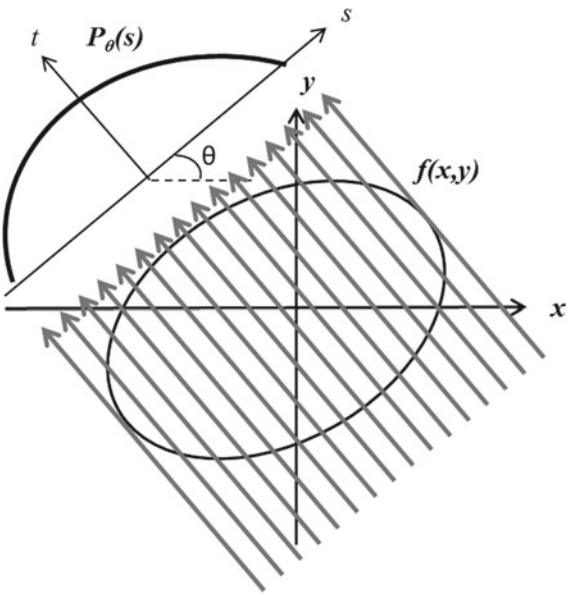

Fig. 5.2 Projection data in parallel beam geometry

Using a delta function, Eq. 5.8 can be re-written as

$$P_\theta(s) = \int_{-\infty}^{\infty}\int_{-\infty}^{\infty} f(x, y)\delta\ (x\cos\theta + y\sin\theta - s)\mathrm{d}x\mathrm{d}y \tag{5.10}$$

The set of line integrals $P_\theta(s)$ are combined to form a projection. The simplest form of projection is a collection of parallel ray integrals as given by $P_\theta(s)$ for a constant θ and is known as parallel projection. The projections can be formed for various angles θ by rotating either the object or the source-detector pair. In the case of neutrons, the source cannot be moved; hence the object (or sample) is rotated. The complete set of projections at various angles is used to deduce cross-sectional information of the object and this technique is known as *tomography*.

5.5 Principles of Neutron Computed Tomography

Tomography is derived from the Greek word '*tomos*' (which means slice or section) and '*graphia*' (which means to draw). Computed Tomography (CT) [2–4] technique is used to obtain cross-sectional information/images of objects. A conventional radiograph is a projection image of the density and thickness variation of the sample. The information along the path of the incident beam is integrated/superimposed in the radiographed and cannot be discerned as such. However, a combination of multiple projection images (radiographs) acquired at various angles can be used to extract features from the complete volume of the object. This technique is known as Computed Tomography. The cross-sectional information is extracted mathematically using various reconstruction methods. The mathematical basis for tomographic imaging was first explained by Radon [5].

Figure 5.3 shows the schematic of data acquisition for transmission tomography. A neutron beam is incident on the sample. The transmitted intensity (radiograph) is recorded by the detector. The sample is rotated using a sample manipulator and the projections (or radiographs) are recorded by the detector for different angles. The set of projections are then used to reconstruct the complete three-dimensional volume of the object on a three-dimensional grid which is discretized into unit cells known as '*voxels*' (short for volume pixels). The reconstructed volume represents the attenuation map of the object.

5.5.1 The Radon Transform

The Radon transform [5] was defined by Johann Radon in 1917. Let $\mathbb{R}^2$ denote the 2D Euclidean space (Fig. 5.4) with a point representation $\overline{x} = (x, y)$ in Cartesian co-ordinate.

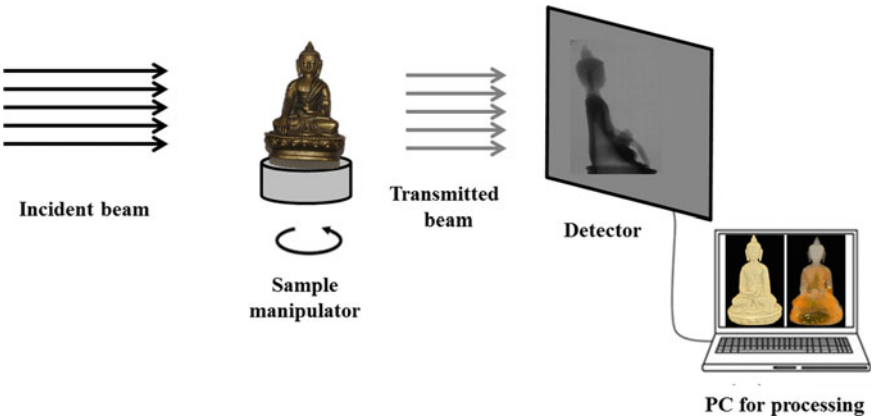

Fig. 5.3 Schematic configuration for transmission tomography

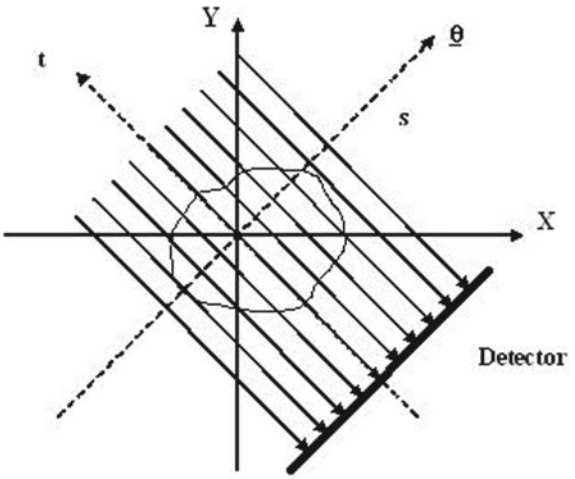

Fig. 5.4 Co-ordinate system for parallel beam projection

In the rotated co-ordinate system (s, t) with axes parallel to vectors $\hat{\theta}(\theta)$ and $\hat{\theta}^{\perp}(\theta)$, we have

$$\begin{pmatrix} s \\ t \end{pmatrix} = \begin{pmatrix} \cos\theta & \sin\theta \\ -\sin\theta & \cos\theta \end{pmatrix} \begin{pmatrix} x \\ y \end{pmatrix} \tag{5.11}$$

and

$$\begin{pmatrix} x \\ y \end{pmatrix} = \begin{pmatrix} \cos\theta & -\sin\theta \\ \sin\theta & \cos\theta \end{pmatrix} \begin{pmatrix} s \\ t \end{pmatrix} \tag{5.12}$$

A function $f(x, y)$ in $\mathbb{R}^2$ is denoted by $f(s, t) = f(x\cos\theta + y\sin\theta, -x\sin\theta + y\cos\theta)$ in the rotated co-ordinate system (s, t), that is the rotation of (x, y) by an angle θ in the counter-clockwise direction.

The integrals of a 2D function $f(s, t)$ along all possible lines is called the (two-dimensional) Radon Transform of $f(s, t)$

$$g(s, \theta) = \int_{-\infty}^{\infty} f(s, t)\mathrm{d}t \tag{5.13}$$

5.5.2 The Fourier Slice Theorem

An important property of the Radon transform is its close correspondence with the Fourier transform.

The Fourier Slice Theorem (also called Central Slice Theorem) [6] states: "The one-dimensional Fourier transform of a projection of a function $f(x, y)$, i.e. the Fourier transform of data along a line through the origin in the Radon space of $f(x, y)$, is same as the data along the same line through the two-dimensional Fourier transform $F(u, v)$ of $f(x, y)$". The principle of Fourier Slice theorem is schematically shown in Fig. 5.5.

The Fourier transform of $g(s, \theta)$ is given by

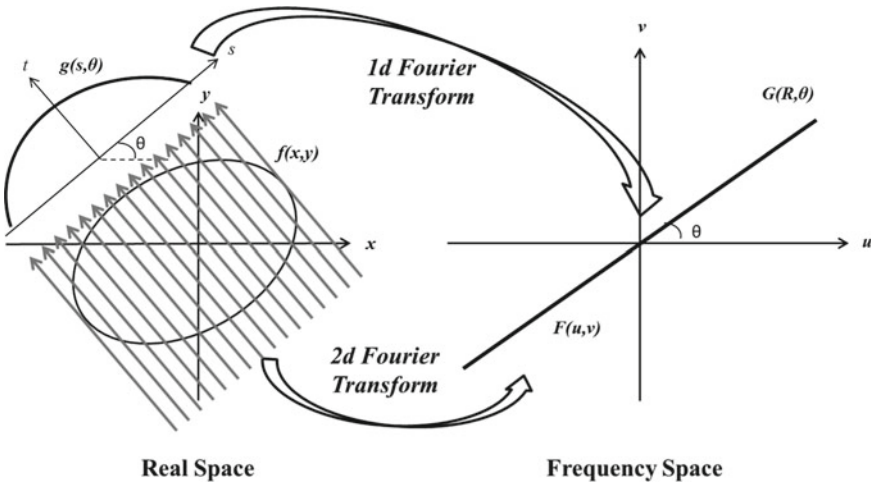

Fig. 5.5 Schematic representation of Fourier Slice theorem

$$G(R,\theta) = \int_{-\infty}^{\infty} g(s,\theta)\mathrm{e}^{-i2\pi Rs}\mathrm{d}s \tag{5.14}$$

Using Eq. 5.12, this becomes

$$G(R,\theta) = \int_{-\infty}^{\infty} \left\{ \int_{-\infty}^{\infty}\int_{-\infty}^{\infty} f(x,y)\delta(x\cos\theta + y\sin\theta - s)\mathrm{d}x\mathrm{d}y \right\} \mathrm{e}^{-i2\pi Rs}\mathrm{d}s \tag{5.15}$$

Changing the order of integration, we get

$$G(R,\theta) = \int_{-\infty}^{\infty}\int_{-\infty}^{\infty} f(x,y)\left\{ \int_{-\infty}^{\infty} \delta(x\cos\theta + y\sin\theta - s)\mathrm{e}^{-i2\pi Rs}\mathrm{d}s \right\} \mathrm{d}x\mathrm{d}y \tag{5.16}$$

The inner integral in Eq. 5.16 contributes under the condition stated in Eq. 5.11. Thus we have

$$G(R,\theta) = \int_{-\infty}^{\infty}\int_{-\infty}^{\infty} f(x,y)\mathrm{e}^{-i2\pi(x\cos\theta + y\sin\theta)R}\mathrm{d}x\mathrm{d}y \tag{5.17}$$

Substituting

$$u = R\cos\theta$$
$$v = R\sin\theta$$

Equation 5.17 becomes

$$G(R,\theta) = \int_{-\infty}^{\infty}\int_{-\infty}^{\infty} f(x,y)\mathrm{e}^{-i2\pi(xu+yv)}\mathrm{d}x\mathrm{d}y = F(u,v) \tag{5.18}$$

Thus it is shown that the 1D Fourier Transform $G(R,\theta)$ of projection data $g(s,\theta)$ is indeed equal to the two-dimensional Fourier transform $F(u,v)$ of $f(x,y)$. This is the Fourier Slice Theorem.

We can rewrite Eq. 5.18 as

$$G(R,\theta) = F(R\cos\theta,\ R\sin\theta) \tag{5.19}$$

5.5.3 Direct Fourier Method

Once $F(u, v)$ is obtained from the Fourier Transform $G(R, \theta)$ of the projection data $g(s, \theta)$ using Fourier Slice Theorem, the function $f(x, y)$ may be calculated using the Inverse Fourier Transform on $F(u, v)$. This is the Direct Fourier reconstruction.

However, there is a catch. The standard Inverse Fourier Transform requires data on a rectangular grid whereas Fourier slice Theorem gives data on a polar grid. For a practical implementation, a complicated frequency space interpolation is required [7, 8].

5.5.4 Backprojection

Let us suppose that the projection data is $g(s, \theta)$. The backprojection operator B may be defined as

$$[Bf](x, y) = \int_{-\pi/2}^{\pi/2} g(s, \theta) \mathrm{d}\theta \tag{5.20}$$

Qualitatively, the backprojection step is akin to "smearing out" the line integral data (projection data) along the same lines in the reconstructed object that produced the line integrals in the original object and adding the data for all the projected rays. However, the quality of the reconstructed image generated depends on the number of projections used. Figure 5.6 shows the effect of number of projections on the final reconstructed image. This is illustrated using a Shepp-Logan phantom [9]. Increasing the number of projections enhances the image contrast and reduces the streaks due to backprojection.

5.5.5 Filtered Backprojection Method

If the reconstruction process consists of backprojection only, the net effect is low-pass filtering which is manifested easily when we have a point object. To compensate for the loss in information related to sharp features on account of low-pass filtering, it is essential to filter the projection data with a high-pass filter before the backprojection step (Fig. 5.7). This forms the basis of filtered backprojection (FBP) scheme. FBP is the most widely used technique for 2D tomography reconstruction.

Mathematically, the high-pass filter is nothing but a ramp filter in the Fourier domain. The filtered backprojection algorithm may be derived as follows. Using inverse Fourier transform on Eq. 5.18, the object function $f(x, y)$ can be expressed as

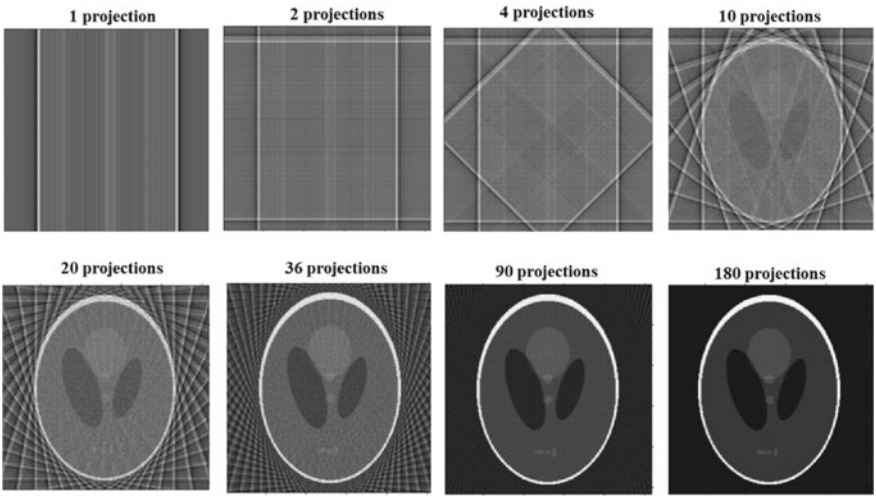

Fig. 5.6 Effect of number of projections on the backprojected image (Illustration uses a Shepp-Logan phantom)

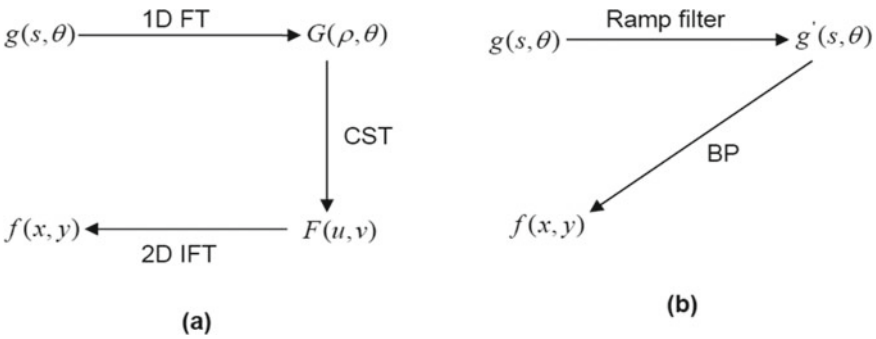

Fig. 5.7 Schematic representation of **a** Direct Fourier Transform. **b** Filtered backprojection

$$f(x, y) = \int_{-\infty}^{\infty} \int_{-\infty}^{\infty} F(u, v) e^{i2\pi(ux+yv)} du dv \tag{5.21}$$

By substituting

$$\begin{aligned} u &= R\cos\theta \\ v &= R\sin\theta \end{aligned} \tag{5.22}$$

Equation 5.21 becomes

$$f(x, y) = \int_0^{2\pi} \int_0^{\infty} G_\theta(R, \theta) \mathrm{e}^{i2\pi R(x\cos\theta + y\sin\theta)} R \mathrm{d}R\mathrm{d}\theta \tag{5.23}$$

where $G_\theta(\cdot)$ is the Fourier function in polar co-ordinates. We can re-write Eq. 5.23 as

$$\begin{aligned} f(x, y) = &\int_0^{\pi} \int_0^{\infty} G_\theta(R, \theta) \mathrm{e}^{i2\pi R(x\cos\theta + y\sin\theta)} R \mathrm{d}R\mathrm{d}\theta \\ &+ \int_0^{\pi} \int_0^{\infty} G_\theta(R, \theta + \pi) \mathrm{e}^{i2\pi R(x\cos(\theta+\pi) + y\sin(\theta+\pi 0)} R \mathrm{d}R\mathrm{d}\theta \end{aligned} \tag{5.24}$$

Using the fact that Fourier function $G_\theta(\cdot)$ is periodic with period 2π

$$G_\theta(R, \theta + \pi) = G_\theta(-R, \theta) \tag{5.25}$$

Using the interval $0 \leq \theta < \pi$ for $-\infty < R < \infty$, Eq. 5.24 may be written as

$$f(x, y) = \int_0^{\pi} \left[\int_{-\infty}^{\infty} G_\theta(R, \theta) |R| \mathrm{e}^{i2\pi R(x\cos\theta + y\sin\theta)} \mathrm{d}R \right] \mathrm{d}\theta \tag{5.26}$$

Using the Fourier slice theorem, the 2D Fourier transform $F_\theta(R, \theta)$ is equal to the 1D Fourier transform of the projection at angle θ, we get

$$\begin{aligned} f(x, y) &= \int_0^{\pi} \left[\int_{-\infty}^{\infty} G_\theta(R, \theta) |R| \mathrm{e}^{i2\pi R(x\cos\theta + y\sin\theta)} \mathrm{d}R \right] \mathrm{d}\theta \\ &= \int_0^{\pi} \left[\int_{-\infty}^{\infty} \left[\int_{-\infty}^{\infty} g(s, \theta) \mathrm{e}^{-i2\pi Rs} \mathrm{d}s \right] |R| \mathrm{e}^{i2\pi(x\cos\theta + y\sin\theta)} \mathrm{d}R \right] \mathrm{d}\theta \end{aligned} \tag{5.27}$$

Equation 5.27 describes the complete filtered backprojection scheme. The projection data $g(s, \theta)$ are Fourier transformed $\left(\int_{-\infty}^{\infty} g(s, \theta) \mathrm{e}^{-i2\pi Rs} \mathrm{d}s\right)$, filtered with a ramp filter $|R|$, inversely Fourier transformed $\left(\int_{-\infty}^{\infty} [\ldots] \ldots \mathrm{e}^{i2\pi R(x\cos\theta + y\sin\theta)} \mathrm{d}R\right)$ and finally backprojected $\left(\int_0^{\pi} [\ldots] \mathrm{d}\theta\right)$.

5.6 Algebraic Reconstruction Techniques

In the algebraic reconstruction technique, the projections are expressed as a set of linear equations. The construction of the attenuation distribution is then obtained by calculating the least squares (LS) solution for the set of equations. The algebraic reconstruction techniques, such as ART, SART, and SIRT are methods for solving the LS problem using different types of iterations.

5.6.1 Image Representation

CT imaging can be described by the following equation:

$$g = Af \tag{5.30}$$

where $g = (g_1, g_2, \ldots, g_M)^T$ is the observable (measured) data, i.e. projections, $f = (f_1, f_2, \ldots, f_N)^T$ is unknown linear attenuation distribution in the object, and A is a $M \times N$ system matrix. Projections are 2D images of 3D objects which are not used directly for analysis. Reconstruction is a procedure used to transform projections to a meaningful 3D distribution of attenuation in the object, and then the reconstructed images are used for analysis. From the mathematical point of view, reconstruction is an inverse problem: the aim is to find unknown f using known g by solving the Eq. (5.30). Therefore, most theories of inverse problems can be applied in the field of tomographic reconstruction.

In an algebraic approach to CT problem, it is assumed that the reconstructed object consists of a matrix of unknowns, and the projection data are modeled by a set of linear equations. The solution of the reconstruction problem is then obtained by the Least Square solution for the set of equations.

5.6.2 Observation Model

Let us consider the vector of linear attenuation coefficients in the pixels $f = (f_1, f_2, \ldots, f_N)^T \in \mathbb{R}^{N\times 1}$. The projection data $g = (g_1, g_2, \ldots, g_M)^T \in \mathbb{R}^{MX1}$ can be expressed as a set of linear equations.

$$\begin{aligned} g_1 &= a_{11} f_1 + a_{12} f_2 + \cdots + a_{1N} f_N \\ g_2 &= a_{21} f_1 + a_{22} f_2 + \cdots + a_{2N} f_N \\ &\vdots \\ g_M &= a_{M1} f_1 + a_{M2} f_2 + \cdots + a_{MN} f_N \end{aligned} \tag{5.31}$$

where ε_i is the additive noise. In matrix notation, Eq. 5.31 can be written as

$$\begin{pmatrix} g_1 \\ g_2 \\ . \\ . \\ g_M \end{pmatrix} = \begin{pmatrix} a_{11} & a_{12} & . & . & a_{1N} \\ a_{21} & a_{22} & . & . & a_{2N} \\ . & . & . & . & . \\ . & . & . & . & . \\ a_{M1} & a_{M2} & . & . & a_{MN} \end{pmatrix} \begin{pmatrix} f_1 \\ f_2 \\ . \\ . \\ f_N \end{pmatrix} \tag{5.32}$$

or

$$g = Af \tag{5.33}$$

For a 2D slice, $N = n_p^2$ is the total number of pixels and $M = n_p \cdot n_\varphi$ is the number of detectors, n_p is the number of pixels in one row of the planar image and n_φ is the number of acquisition angles. The matrix $A \in \mathbb{R}^{M \times N}$ is called the observation matrix or the probability system matrix. The matrix element a_{ij} is the path traveled by the neutron in the ith pixel when the neutron is detected by the jth projection bin.

If the matrix A is modeled correctly it includes all the physical features of the detecting system. Forming projection bins as a linear combination of attenuation coefficients is clearly a discrete version of integrating attenuation coefficients over some path length as presented in Eq. 5.31.

5.6.3 The Linear Least Square Estimation

Equation 5.33 can be solved using linear least square (LS) estimation. Our aim is to solve the estimate $\hat{f}_{LS}$ satisfying the condition

$$\hat{f}_{LS} = \arg\min \|g - Af\| \tag{5.34}$$

Knowing the projection data g and constructing the probability system matrix A, our task is to solve the LS problem denoted by Eq. 5.34. The observation model is mostly under-deterministic, that is, $N > M$. In such a case, the LS problem has no unique solution and some of the solutions must be chosen based on constraints. Most commonly, the minimum norm solution is used. Furthermore, the inverse problem of CT is usually ill-posed and some regularization may be needed in solving the LS problem. In addition, the matrix A is usually very large and the LS solution must be computed iteratively.

5.6.4 Implementation of ART

To implement the algorithm for computation, an initial guess of the solution is required. This guess, denoted by $f_1^{(0)}, f_2^{(0)}, f_3^{(0)}, \ldots, f_N^{(0)}$, may be assigned a value of zero or an average value of the projection sum to all the initial f_i's. The reconstruction process may be expressed mathematically as follows:

$$f_j^{(k)} = f_j^{(k-1)} + \frac{g_i - \sum_{j'=1}^{N} f_{j'}^{(k-1)} a_{ij'}}{\sum_{j'=1}^{N} a_{ij'}^2} a_{ij} \tag{5.35}$$

In Eq. 5.35, g_i is the measured ray-sum along the ith ray. The term $\sum_{j=1}^{N} f_j^{(k-1)} a_{ij}$ may be considered to be the computed ray-sum for the same ray based on the $(k-1)$th iteration. The correction Δg_i to the jth cell is obtained by first calculating the difference between the measured ray-sum and the computed ray-sum, normalizing this difference by $\sum_{j=1}^{N} a_{ij}^2$ and then assigning this value to all the image cells in the ith ray, each assignment being weighted by the corresponding a_{ij}.

There are different variants of ART. These algorithms differ in the manner in which corrections are applied and are presented here in brief.

5.6.5 Additive ART

The additive ART or simple ART algorithm was originally proposed by Gordon [10] for CT reconstruction. In this method, corrections are applied to all the voxels through which the ith ray passes, before calculating the correction for the next ray. The correction applied to jth cell of the object grid for ith ray is computed as [4, 11–13]

$$\hat{f}_j^{(k)} = \hat{f}_j^{(k-1)} + \lambda \frac{a_{ij} \Delta g_i}{\alpha_i} \tag{5.36}$$

where $\Delta g_i = g_i - \hat{g}_i$, $\alpha_i = \sum_{j=1}^{N} a_{ij}^2$ and λ is a relaxation parameter and $\lambda < 1$.

ART reconstruction usually tend to be noisy due to approximations introduced in the evaluation of a_{ij}'s. The reconstruction thus results in poor approximations of corresponding ray-sums. The effect of noise can be reduced by using the relaxation parameter λ.

5.6.6 Simultaneous Iterative Reconstruction Technique (SIRT)

In simultaneous iterative reconstruction technique (SIRT), the elements of the unknown function f_j for a particular cell are modified after all the correction values corresponding to individual rays have been calculated. The correction applied to jth cell of the object grid is computed as

$$\hat{f}_j^{(k)} = \hat{f}_j^{(k-1)} + \sum_{i=1}^{N_{c_j}} \lambda \frac{a_{ij} \Delta g_i}{\alpha_i} \tag{5.37}$$

The algorithm is similar to additive ART but the correction $\Delta g_i = g_i - \hat{g}_i$ is applied for all the ith rays before moving on to the next cell. This usually results in smoother reconstructions at the expense of slower convergence rates.

5.6.7 Simultaneous ART (SART)

The SART method was invented by Anderson and Kak [2, 14]. It connects advantages of ART and SIRT algorithms. It was found to be very efficient, accurate and superior in implementation [2, 11, 12, 14]. It yields good quality reconstruction with single iteration.

For each projection angle θ, the correction is applied to the jth cell sequentially for all ith rays as follows:

$$\hat{f}_j^{(k)} = \hat{f}_j^{(k-1)} + \lambda \frac{a_{i_\theta j}\left(g_{i_\theta} - \hat{g}_{i_\theta}\right)}{\sum_{j=1}^{N} a_{i_\theta j}^2} \tag{5.38}$$

One iteration is completed when all ith rays have been used exactly once. Since SART updates the values of cells in the image for each projection angle, it is well suited for GPU-based corrections. However, SART is slightly slower than ART in terms of computational time, due to the voxel-based pooling of correction terms.

5.7 Energy-Resolved Neutron Imaging

Energy resolved neutron imaging techniques comprise of experiments where specific energy is selected (using double crystal monochromator [15] or time-of-flight method [16] or mechanical velocity chopper [17]) to form an image corresponding to a single energy. In this way, neutron images can be formed single energies over the entire neutron spectrum, and we can obtain an image stack of energy-resolved images for

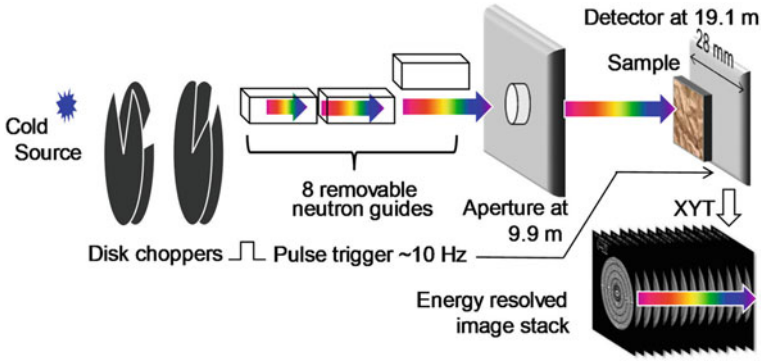

Fig. 5.8 Schematic of energy-resolved neutron imaging experimental setup at Bilby beamline, Australian centre for neutron scattering (reproduced from [18] with permission from AIP publishing)

the same object. Figure 5.8 shows the schematic of an energy-resolved experimental setup at Bilby beamline, Australian Centre for Neutron Scattering [18].

The selection of energy in a continuous neutron spectrum source (such as reactor source) can be implemented using a monochromator or velocity chopper system. However, this is achieved at the cost of reduced neutron intensity as a small fraction of the available neutrons are only utilized to achieve high wavelength resolution for a relevant bandwidth. The use of pulsed neutron sources (like spallation sources) can offer high spectral resolutions with large wavelength ranges without any additional penalty on neutron intensity.

One of the most popular energy-resolved technique is the neutron Bragg edge imaging [19, 20]. Neutron Bragg edge imaging enables spatially resolved studies of crystalline structures by exploiting the Bragg edges in the transmission spectra recorded in each pixel of an imaging detector. Bragg edges in the transmission spectrum are the signature of Bragg scattering from polycrystalline materials. For a given crystal lattice family hkl, with lattice spacing d_{hkl}, the scattering angle increases with the wavelength (λ) upto $\lambda = 2d_{\mathrm{hkl}}\sin(\pi/2)$. Beyond this wavelength, the Bragg condition cannot be satisfied any longer, which results in a sharp drop of the attenuation of the material, called the Bragg edge.

Figure 5.9 shows the total cross-section for different polycrystalline materials and the associated Bragg edges. Thus, the analysis of the Bragg edges allows for the characterization of crystalline features of materials such as lattice strains or phase fractions. The Bragg cut-offs for many crystal materials are in this energy range that allows radiography contrast variations by applying energy-selective imaging techniques.

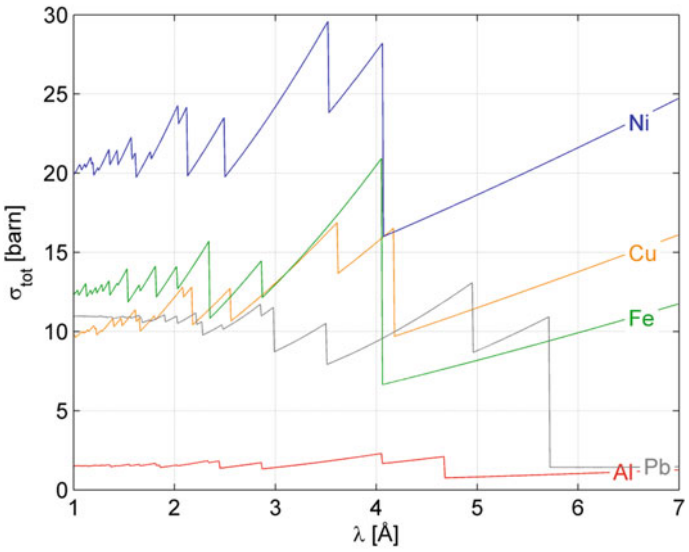

Fig. 5.9 Total cross-section and the associated Bragg edges for different polycrystalline materials

5.8 Summary

Neutron radiography and neutron tomography and its related neutron imaging techniques have established themselves as invaluable non-destructive inspection methods and quantitative measurement tools. The focus of this chapter has been to understand the mathematics of neutron image formation and methods for volumetric measurements using computed tomography and related reconstruction methods. The focus has been primarily related to the estimation of macroscopic material interaction cross-sections which is the goal of image analysis. A discussion of volumetric reconstruction techniques using analytic or iterative computed tomography algorithms has been done.

References

1. https://www.eichrom.com/wp-content/uploads/2018/02/Neutron-Attenuation-White-Paper-by-D-M-rev-2-1.pdf
2. Kak AC, Slaney M (1987) Principles of computerized tomographic imaging. IEEE Press
3. Herman GT (1980) Image reconstruction from projections: the fundamentals of computerized tomography. Academic Presss
4. Natterer F (1986) The mathematics of computerized tomography. Wiley, New York
5. Radon J (1917) On the determination of functions from their integrals along certain manifolds [in German]. Math Phys Klass 69:262–277

6. Haykin S (ed) (1985) Tomographic imaging with diffracting and non-diffracting sources. In: Array signal processing, Prentice-Hall, Englewood Cliffs, NJ
7. Stark H, Woods JW, Paul I, Hingorani R (1981) Direct Fourier reconstruction in computer tomography. IEEE Trans Acoust Speech Signal Process ASSP-29:237–244
8. Jacobsson C (1996) Fourier methods in 3D-reconstruction from cone-beam data. Ph. D. Thesis, Linkoping University
9. Shepp LA, Logan BF (1974) The Fourier reconstruction of a head section. IEEE Trans Nucl Sci NS-21:21–43
10. Rangayyan R, Prakash A, Gordon R (1985) Algorithms for limited view computed tomography: an annotated bibliography and challenge. Appl Opt 24(23):4000–4012
11. Chlewicki W (2001) 3D simultaneous algebraic reconstruction technique for cone-beam projections. Master of Science Thesis
12. Mueller K (1998) Fast and accurate three-dimensional reconstruction from cone-beam projection data using algebraic methods. Ph. D. thesis, The Ohio State University
13. Seppnen AO (2000) Correction of collimator blurring and attenuation in single photon emission a computed tomography. Master of Science thesis, University of Kuopio, Faculty of Natural and Environmental Sciences Physics Medical Physics
14. Anderson AH (1989) Algrebraic reconstruction in CT from limited view. IEEE Trans Med Imag 8(1):50–55
15. Schulz M, Boni P, Calzada E, Muhlbauer M, Schilinger B (2009) Energy-dependent neutron imaging with a double crystal monochromator at the ANTARES facility at FRM II. Nucl Inst Methods Phys Res A 605:33–35
16. Kockelmann W, Frei G, Lehmann EH, Vontobel P, Santisteban J (2007) Energy-selective neutron transmission imaging at a pulsed source. Nucl Inst Methods Phys Res A 578:421–434
17. Friedrich H, Wagner V, Wille P (1989) A high-performance neutron velocity selector. Physica B 156&157:547–549
18. Tremsin AS, Sokolova AV, Salvemini F, Luzin V, Paradowska A, Muransky O, Kirkwood HJ, Abbey B, Wensrich CM, Kisi EH (2019) Rev Sci Instrum 90:035114
19. Josic L, Lehmann E, Kaestner A (2011) Nucl Instrum Methods Phys Res 651:166–170
20. Peetermans S, Bopp M, Vontobel P, Lehmann EH (2015) Phys Proc 69:189–197